POLITECNICO DI TORINO
Repository ISTITUZIONALE

A Smart Combined Wireless Sensor Network for Vibration and AE Signals Measurement

Original
A Smart Combined Wireless Sensor Network for Vibration and AE Signals Measurement / Zhang, Z., Lombardo, L., Shi, T., Han, X., Parvis, M., Li, J.. - In: IEEE TRANSACTIONS ON INSTRUMENTATION AND MEASUREMENT. - ISSN 0018-9456. - STAMPA. - 74:(2025), pp. 1-12. [10.1109/tim.2025.3551572]

Availability:
This version is available at: 11583/3004516 since: 2025-10-29T09:47:52Z

Publisher:
IEEE

Published
DOI:10.1109/tim.2025.3551572

Terms of use:

This article is made available under terms and conditions as specified in the corresponding bibliographic description in the repository

Publisher copyright
IEEE postprint/Author's Accepted Manuscript

©2025 IEEE. Personal use of this material is permitted. Permission from IEEE must be obtained for all other uses, in any current or future media, including reprinting/republishing this material for advertising or promotional purposes, creating new collecting works, for resale or lists, or reuse of any copyrighted component of this work in other works.

(Article begins on next page)

16 November 2026

A Smart Combined Wireless Sensor Network for Vibration and AE Signals Measurement

Zhaoyu Zhang, Luca Lombardo, *Member*, *IEEE*, Tianyi Shi, Xutao Han, Marco Parvis, *Fellow, IEEE*, Junhao Li, *Senior Member, IEEE*

***Abstract*—Mechanical and insulation defects can lead to severe faults in power equipment, making it essential to conduct a comprehensive and accurate fusion diagnosis. Vibration and acoustic emission (AE) are two effective ways to detect the above two defects. This paper proposes and develops a reliable smart vibration and AE combined wireless sensor network (WSN), featuring both low cost and power consumption, which is suitable to detect and monitor the power equipment's mechanical and insulation conditions. Firstly, the combined sensor is designed and the feasibility is validated by simulation, then the circuit system is designed in order to sample and process analog signals, perform edge computing, self-calibrate impedance and transmit wireless data. The calibartion and consumption tests are carried out to verify the combined measurement performance and reliable smart sensing. Then, a combined vibration and AE WSN is designed and established, enabling efficient sensor control. Fixed and mobile clients are proposed to support monitoring for various applications. Additionally, laboratory experiments demonstrate the sensor's ability to synchronously measure vibration and partial discharge (PD), a novel vibration-AE amplitude graph is presented to reflect the correlation between vibration and PD. The proposed WSN has been deployed in an actual GIS substation, it is able to detect an apparent abnormal vibration on phase-B of the voltage transformer chamber due to a poor electrical contact defect. This paper presents a reliable and effective wireless sensing approach for the distributed fusion detection and diagnosis of both mechanical and insulation conditions of power equipment, offering a feasible solution for industrial automated measurement.**

***Index Terms*—Smart sensor, Wireless Sensor Network, mechanical vibration, partial discharge, acoustic emission**

I. INTRODUCTION

Distributed measurement systems and Wireless Sensor Networks (WSN) are applied in several fields such as smart home automation, public security and cultural heritage [1, 2]. The large capabilities and flexibility of these systems are attracting an ever-growing attention of scholars. Nevertheless, few solutions are nowadays available for the continuous monitoring and detection of mechanical and insulation defects in power equipment.

Manuscript received xxx; revised xxx; accepted xxx. This work is supported by Guangdong Provincical Key Laboratory of Electric Power Equipment Reliability Open Fund 2023 (GDDKY2023KF02). *(Corresponding author: Junhao Li.)*

Zhaoyu Zhang, Tianyi Shi, Xutao Han and Junhao Li are with the State Key Laboratory of Electrical Insulation and Power Equipment, Xi'an Jiaotong University, Xi'an 710049, China (e-mail: junhaoli@mail.xjtu.edu.cn).

Zhaoyu Zhang, Luca Lombardo and Marco Parvis are with the Department of Eletronics and Telecommunications, Politecnico di Troino, 10129 Turin, Italy.

The mechanical and insulation defects are two main causes of serious fault in large power equipment, such as gas insulated switchgear (GIS), transformer, generator, etc. [3-6], and any damage would be severe once the fault occurs. Vibration and AE are generally measured to detect mechanical and insulation defects with good performance, however, they are differently sensitive to some specific defects [7-11]. For instance, GIS is a high-voltage, high-current transmission and transformation power equipment characterized by its large size, long circuits, and complex structure. The structure of the GIS disconnector is shown in Fig. 1, frequent operations could lead to poor contact with abnormal vibration, and the contact friction produce the metal particles on grounded enclosure, which can be attracted by the high voltage busbar to jump generating AE signal or cause flashover under impact vibration from switching operation [12-14]. Some particles adhered on basin-type insulator can even induce creeping discharge [15]. Therefore, the characteristics and position of the defect determine which detection signal is more suitable, and the combined measurement for vibration and AE make diagnosis comprehensive.

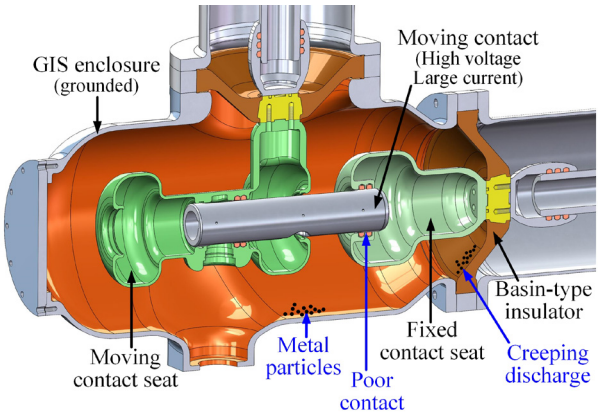


Fig. 1. The structure of common disconnector in GIS.

The fusion measurement and analysis of multi-signal for equipment defect detection is an important study topic [16]. In [17] A. Stief, et al. analyzed acoustic, electric, and vibration signals gathered from induction motors operating under different conditions to diagnose both electrical and mechanical faults applying the fusion approach based on the combination of a two-stage Bayesian method and Principal Component Analysis (PCA). Siyu Shao, et al. proposed a Deep Learning-Convolutional Neural Network (DCNN) method to diagnose

induction motor fault with vibration and current signals [18]. Fusion signal analysis has been verified to deliver more accurate and stable detection than conventional methods. However, the lack of practical and feasible combined sensors hinders its application in real-world measurement scenarios [19-21]. Shuang Li et al. developed a vibration-temperature sensor for high-temperature environments, addressing the issues of measurement instability and temperature drift in traditional sensors at 800°C [22]. Haotian Wang et al. proposed a novel composite sensor for GIS, capable of detecting PD and measuring overvoltage, aimed at enhancing insulation condition evaluation [23]. Combined sensors are efficient in detecting a single type of defect, but research on fusion measurement for detecting typical insulation and mechanical defects is limited. While improving detection accuracy, the detection scope (comprehensiveness) should also be emphasized.

Traditional measurement systems for defect and fault detection in power equipment typically rely on wired sensors, which are impractical for continuous on-site monitoring. Additionally, these systems generally focus on the measurement and analysis of a single signal. As a result, the efficiency of industrial maintenance is very low. Nowadays, with the development of Fourth Industrial Revolution, advanced measurement is currently evolving to be wireless, distributed, multi-signal, smart, making extensive use of fusion analysis and artificial intelligence. X. Zhao proposes a novel and deployable edge device that utilizes a feature-based Tiny Machine Learning (Tiny ML) model for vibration data processing and machine condition monitoring, while maintaining modeling generalizability and computing efficiency [24]. In [25], multiscale analysis of motor vibration and stator current signals is proposed as a deep-learning-based model named multiresolution & multisensor fusion network. In [26], a novel edge collaborative compressed sensing for mechanical vibration monitoring (MVM) is presented to address the severe shortage of storage and computational resources and long delay in transmitting massive vibration data in WSN for MVM. A novel intelligent diagnosis method based on Multisensor Fusion (MSF) and Convolutional Neural Network (CNN) is explored in [27]. Most research focuses on Artificial Intelligence (AI) algorithms. However, measurement is the premise of analysis and diagnosis. There are a few reports about reliable wireless combined sensor and network systems for evaluating the mechanical and insulation conditions of power equipment.

This paper, starting from the preliminary design of the wireless sensing node, develops a smart combined wireless sensor network for measuring vibration and AE signals, which can be applied to detect mechanical and insulation defects in power equipment at transformer substations or other plants. The major novelties and scientific contributions include:

1) The wireless smart vibration and AE combined sensor is designed and developed for detecting mechanical and insulation defects in GIS equipment, featuring reliable measurement, edge computing, wireless transmission, and impedance self-calibration capabilities.

2) A wireless sensor network is designed and implemented for distributed detection of GIS substation equipment, introducing two online monitoring modes (fixed and mobile clients) in addition to the general detection mode.

3) The metal particle discharge and vibration combined experiments are implemented in laboratory, a firstly proposed VAA graph can describe the correlation between vibration and PD. The application in actual GIS substation verifies the reliability and stability of the WSN.

The development and performance tests of the wireless sensor are presented in section II and section III respectively. The design and implementation of the WSN is introduced in section IV. The vibration-PD experiment in laboratory and the application in GIS substation are discussed in section V. and the conclusions are summarized in Section VI.

This paper is an extension of the proceedings paper (ID number: 1570978495) published on I2MTC 2024 [28].

II. Development of The Wireless Sensor

Choosing a suitable wireless technology is the primary concern. Currently, various wireless transmission technologies exist, each with its own characteristics [29]. The performance comparison of four commonly used wireless transmission technologies is shown in TABLE I. The throughput of Wi-Fi is the fastest (0.6 ~ 7 Gbps), and the range reaches from 30 to 100 m, but its power consumption and cost are high, so it is usually powered stably and applied as public networks (entertainment or office) and video streaming,, etc. Though the communication range of Bluetooth Low Energy (BLE) is within 10 ~ 50 m, it offers moderate throughput (1 ~ 3 Mbps), low power consumption, low cost, and low latency, which makes it suitable for application in home automation, Personal Area Networks (PAN), and positioning. Lora is featured by very low power consumption and long range (up to 10 km), yet the throughput is very low (0.3 ~ 50 kbps) and sometimes it delays, hence it is used in applications with large areas and small amounts of data, such as environmental monitoring, smart cities, and agriculture. ZigBee is good at scalability, it can make mesh network between devices, so it is employed in small area communication with numerous devices, such as Internet Of Thing (IoT), building automation and energy management (smart meters).

TABLE I
Comparison of the Four Main Wireless Technologies

Protocol	Wi-Fi	BLE	LoRa	ZigBee
Throughput	0.6 ~ 7 Gbps	1 ~ 3 Mbps	0.3 ~ 50 kbps	20 ~ 250 kbps
Range / m	30 ~ 100 m	10 ~ 50 m	0.1~ 10 km	10 ~ 75 m
Power consumption	High	Low	Very Low	Low
Scalability	Middle	Middle	Middle	High
Cost	High	Low	Middle	Middle
Latency	Low	Low	Middle	Low

The research object of this paper is the combined and distributed vibration and AE WSN for large electrical

equipment which works in transformer substation, requiring good throughput, low power consumption and latency. Despite BLE is short at transmission range, this can be addressed by adding clients, and BLE 5.x has a flexible balance between throughput and range (2M PHY-high speed, LE Coded PHY-long range), so it is a relative comprehensive solution.

The proposed wireless sensor comprises two main components, a developed vibration-AE combined sensor and a multifunction integrated Printed Circuit Board (PCB).

A. Physical design

Since piezoelectric vibration sensors share the same structure with AE sensors and operate at different bands, it is possible to make a combined sensor whose output signal includes both vibration (< 4 kHz) and AE (> 20 kHz) information [30-31]. The proposed sensor is shown in Fig. 2.

The acoustic matching layer increases acoustic transmissivity for AE measurement and works as the base for vibration measurement. The PZT-5 element realizes the conversion between vibration, AE and voltage due to its excellent piezoelectric property. The backing can attenuate the noise from echo and broaden the AE response band, it is embedded in a metal mass which provides inertia for vibration measurement. The sensing node design is completed by a dedicated PCB which is mounted inside the enclosure consisting of analog processing circuit, microcontroller with integrated BLE transceiver, RF antenna and matching circuit.

To verify the feasibility of the sensor and confirm its response parameters, a Finite Elements Analysis (FEA) is employed to calculate the sensitivity of vibration and AE.

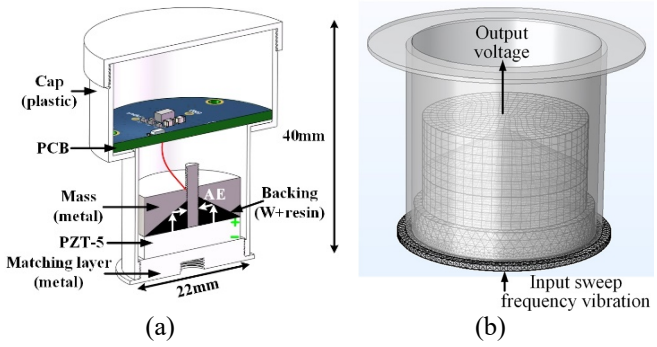


Fig. 2. The sensor structure. (a) Structure design. (b) FEA model.

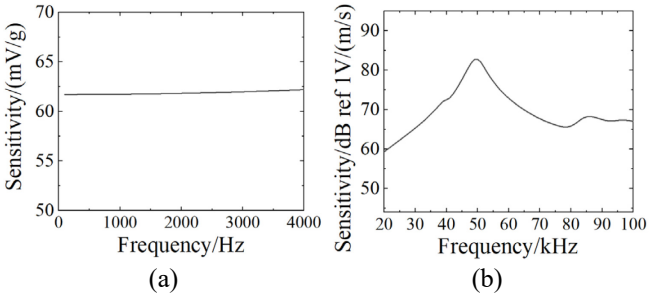


Fig. 3. The simulation results. (a) Vibration sensitivity. (b) AE sensitivity.

The physical parameters are determined by theoretical calculation of our previous work and set in this simulation [32]. Since the sensor is designed for defect detection of GIS, the vibration and AE measurement bands should be 100 Hz ~ 4 kHz and 20 kHz ~ 100 kHz. The results of the simulation are shown in Fig. 3. It is known that the vibration sensitivity reaches 62 mV/g (g=9.8 m/s^2) under 4 kHz (Fig. 3 (a)). The AE sensitivity rises from 59 dB at 20 kHz to 84 dB at 50 kHz (resonant frequency), then declines down to around 65 dB. Generally, under one fifth of the first resonant frequency is vibration measurement band which performs stable response, and the resonant frequency could provide good response for AE measurement. Therefore, the sensor can effectively acquire both vibration and AE signals simultaneously.

B. Electronic design

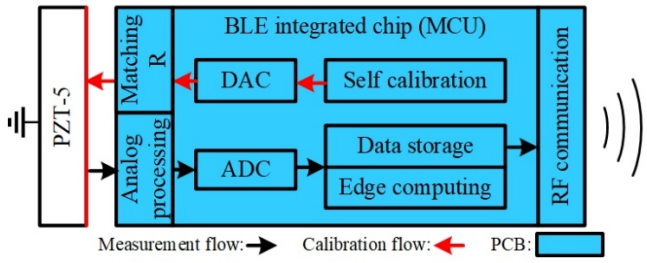


Fig. 4. Technical frame of the wireless sensor.

The technical frame of the sensor is described in Fig. 4. The BLE system-on-chip (EFR32MG24) is the core part of the circuit which enables the sensing node to acquire and store data, make impedance calibration, implement edge computing and RF communication with BLE 5.3 protocol. The chip provides high-performing ADC and DAC peripherals together with a very low power consumption and high computing capability, making it an ideal choice for high-performing integrated sensing applications. During a measurement, the analog signal from PZT-5 is conditioned and then converted to digital signal by ADC, after storage and processing, it is transmitted by the BLE transceiver. For impedance self-calibration, the DAC generates excitation signal on PZT-5 through a matching resistor, simultaneously, the signal on PZT-5 is acquired by measurement chain.

The designed PCB is shown in Fig. 5 (a), it has a diameter of 33 mm. Since the sensor is supplied by a 3 V coin cell battery (CR2477), the static input signal of ADC should be shifted to half of the supply (around 1.5 V) to collect bipolar signal from the PZT-5. Additionally, the high impedance of PZT-5 needs to be converted to low to prevent unacceptable signal degradation. A dedicated analog conditioning circuit is designed for this purpose, as shown in Fig. 5 (b).

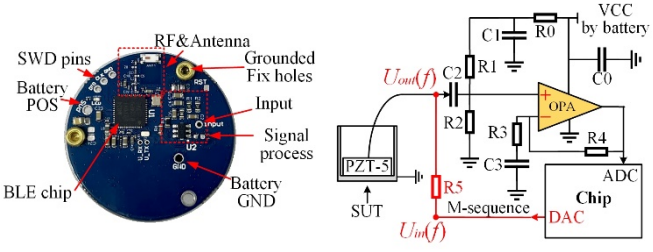


Fig. 5. PCB design. (a) The PCB. (b) Analog conditioning circuit (black) and impedance self-calibration (red) circuit.

Specifically, R0, C1 are used to stabilize the voltage that supplies the operational amplifier (OPA), and a middle-rail voltage (about VCC/2) is obtained through a simple voltage divider (R1, R2) to realize the required DC shift. C2 blocks the DC component from the sensor. R4 and R3 determine the signal gain (set to 10 in this paper). R5 works as a matching resistor for impedance response self-calibration. All component values are displayed in TABLE II.

TABLE II
PARAMETERS OF THE ANALOG PROCESSING CIRCUIT

Components	Value	Components	Value
R0	1 kΩ	C0	200 μF
R1	10 MΩ	C1	100 μF
R2	10 MΩ	C2	10 μF
R3	50 kΩ	C3	10 μF
R4	450 kΩ	R5	5 kΩ

C. Self-Calibration

The vibration or AE sensitivity curve of piezoelectric sensors is actually a kind of frequency response curve, which is related to the impedance response curve of the sensor. Impedance analyzer is often applied to acquire impedance curve, but that is costly and inconvenient. Alternatively, white noise is ideal excitation signal since its power distributes uniformly over the entire bandwidth, but it can not be generated easily. To this aim, pseudorandom binary M-sequence, a periodic sequence owing similar probability properties with discrete binary white noise [33], can be used to get the impedance curve of the designed sensor quickly and without the employment of expensive instrumentation.

The impedance self-calibration chain (red line) is shown in Fig. 4 (b), M-sequence signal, as $U_{in}(f)$, can be generated directly by the DAC on the chip and applied through a matching resistor (10 kΩ) to the PZT-5. Meanwhile, the ADC is utilized to acquire the $U_{out}(f)$. The M-sequence measurement band can be set up by adjusting its clock frequency. Since 100 Hz ~ 100 kHz is our calibration band, the clock frequency (f_{cp}) should be 300 kHz according to M-sequence measurement bandwidth (f_m) equation:

$$f_m \approx \frac{f_{cp}}{3} \tag{1}$$

Fig. 6 (a) demonstrates the M-sequence signal in time domain and frequency domain. Impedance curve $Z(f)$ could be calculated by Eq. (2), where f is the specific frequency, $U_{out}(f)$ and $U_{in}(f)$ represent the voltage amplitudes of the output and input, respectively. R_m is the matching resistor.

$$Z(f) = R_m \frac{U_{out}(f)}{U_{in}(f) - U_{out}(f)} \tag{2}$$

It is depicted in Fig. 6 (b) that the impedance response curves measured by frequency sweep method and M-sequence method match very well, although the latter is characterized by some fluctuations.

The time consumed by frequency sweep method is 1 min for 120 samples, however, M-sequence method requires only 6.823 ms for 500 samples. On the other hand, the energy consumed by M-sequence method is very low, which makes this approach very suitable for self-calibration on battery-powered BLE wireless sensors. The obtained impedance response curve could be used to reflect the output response change caused by dielectric characteristic change [34].

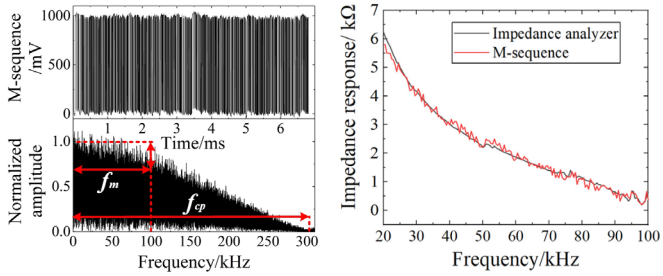


Fig. 6. Self-calibration implementation. (a) The M-sequence signal. (b) Calibration result.

D. Edge computing

Considering the characteristics of the mechanical vibration (<4 kHz) and partial discharge AE (>20 kHz) fusion signal measured by the combined sensor, the fundamental architecture of edge computing proposed in this paper is demonstrated in Fig. 7. Firstly, the fusion signal in time domain should be separated to vibration by downsampling (Extract 1 every 10), and AE signal by high pass filter. The vibration signal, transformed by FFT, provides key vibration information in the frequency domain including amplitude and phase, which are essential for vibration analysis. Additionally, the AE signal (PD) can be recorded to obtain statistical information, such as the number, amplitude and timing of partial discharges, which are valuable for insulation analysis. Furthermore, with the vibration amplitudes and PD amplitudes, it is able to draw the Vibration-AE Amplitude (VAA) graph discussed in section V, which is significant for fusion analysis of the PD associated with vibration.

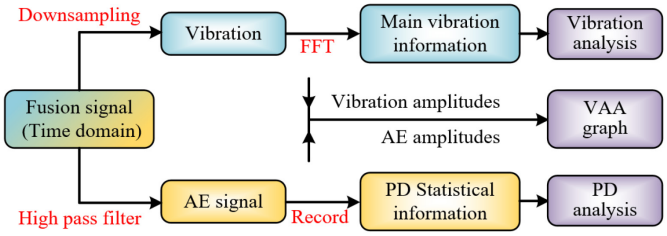


Fig. 7. Fundamental architecture of the combined sensor edge computing.

The edge computing is a kind of embedded system development, because the chip memory is finite, and excessive operation takes time and energy, the calculation procedure should be efficient and lightweight. FFT and high pass filter are two important parts of the combined sensor edge computing. As for FFT, we utilize a radix-2 divide-and-conquer FFT algorithm, breaking the input into even and odd parts to reduce multiplications, and the butterfly operation can efficiently combine frequency components with a complexity of O (N log$N$). For the high-pass filter, the Chebyshev Type-II filter is

suitable due to its lower computational complexity achieved by feedback, and its superior stopband attenuation characteristics, these allow it to realize rapid stopband decay with a low filter order. The high pass filter should effectively separate AE signal from the fusion signal, so the cutoff frequency is set 10 kHz, and the minimum attenuation of stop band is set 40 dB.

Performance of the FFT and the high pass filter are shown in Fig. 8. For the FFT, taking the signal $x(t)=100\sin(2000\pi t)$ as an example, the result accurately shows a 100 mV amplitude and a -90° phase shift at 1 kHz. Concerning the high pass filter, the parameters of the designed 5th-order Chebyshev type-II filter are shown in TABLE III, and the frequency response is displayed in Fig. 8 (b) with a minimum attenuation of 40 dB in the stopband and a stopband cutoff frequency of 10 kHz. The result of the signal separation is shown in Fig. 17.

TABLE III
PARAMETERS OF THE DESIGNED CHEBYSHEV TYPE-II FILTER

Denominator coefficients	Value	Numerator coefficients	Value
1	1	1	0.856573
2	-4.683747	2	-4.276779
3	8.790638	3	8.5474797
4	-8.26336	4	-8.5474797
5	3.8902	5	4.276779
6	-0.733717	6	-0.856573

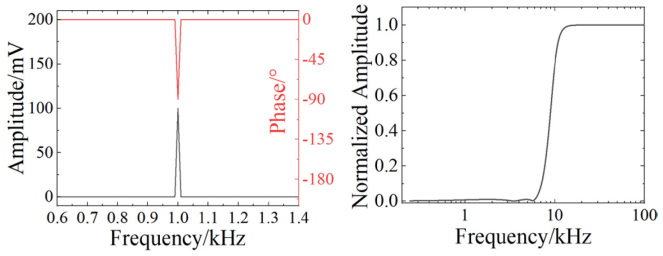


Fig. 8. Performance of the FFT and the high pass filter. (a) The FFT result of the signal: $x(t)=100\sin(2000\pi t)$. (b) Frequency response of the high pass filter.

The assembled prototype of the wireless sensor is shown in Fig. 9, which is featured by:

1) Simultaneous collection of vibration and AE signals.
2) BLE 5.3 with battery supply (CR 2477, 1 A·h).
3) Data rate can be set up to 2 Mbps (1.35 Mbps is practical).
4) The sampling rate can be set up to 2 MHz.
5) The 32-bit ARM Cortex®-M33 core and MCU peripherals could realize edge computing and impedance self-calibration.

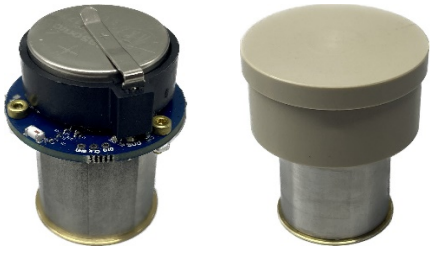


Fig. 9. Smart vibration-AE combined wireless sensor. (a) The wireless sensor (without cap). (b) The assembled sensor.

III. PERFORMANCE TESTS OF THE WIRELESS SENSOR

A. Vibration and AE Calibration

The vibration and AE relative calibration platforms are established in our previous work according to ISO 16063-21:2003 and ISO 12714:1999 respectively in Fig. 10 (a) and (b), RS means Reference Sensor, SUT means Sensor Under Test [32]. For vibration calibration, the two sensors are installed face to face on one vibrator to acquire the same vibration signal; for AE calibration, the sensors are symmetrically installed on the surface of a steel block, with the center excited by a broken lead to generate surface acoustic waves [30-31]. The calibration results are shown in Fig. 10 (c) and (d). Vibration sensitivity reaches around 510 mV/g, while AE sensitivity fluctuates between 70 dB ~ 90 dB and the lowest value is 71.5 dB at 95 kHz. The fluctuation exists due to the uncertainty in calibration, including RS performance, aperture effect, etc. Generally, the uncertainty may cause slight local fluctuations in the frequency response, but it does not significantly affect the overall result.

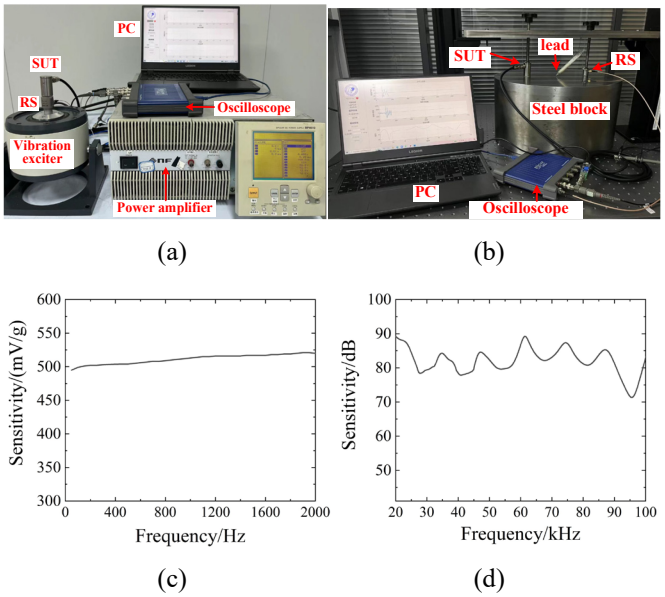


Fig. 10. Calibration experiment. (a) Vibration calibration. (b) AE calibration. (c) Vibration sensitivity. (d) AE sensitivity.

B. Data Rate

Data rate performance is of paramount importance for wireless measurement, especially for real time applications. There are several factors affecting data rate of the wireless sensor, environment, distance, transmission parameters setting, sensor number are four main factors. Regarding transmission parameters, larger packets improve the data rate, but may cause packet loss; wider bandwidth supports higher data rates, but increases interference. In this paper, to acquire good and stable data rate, the packets size is set 240 bytes, bandwidth is 2 MHz. For multiple sensors to one client, as the sensor number increases, the data rate decreases due to shared communication resources of the client. Therefore, multi-to-multi transmission is designed and discussed in Ch. IV. Sec. B. In addition, the device power, performance and signal interference could also affect the data rate. In this section, the

sensor is tested both indoors and outdoors, with the distance between it and the client ranging from 1 m to 20 m. The tested data rates are presented in TABLE IV.

TABLE IV
DATA RATE TEST RESULT OF THE WIRELESS SENSOR

Distance	Data Rate	
	Indoor	***Outdoor***
1 m	1.35 Mbps	1.31 Mbps
4 m	1.17 Mbps	1.05 Mbps
8 m	1.1 Mbps	1.01 Mbps
12 m	1.058 Mbps	887.5 kbps
16 m	653.2 kbps	545.2 kbps
20 m	565.7 kbps	344.8 kbps

It is evident that the data rate drops as the distance increases weather indoors or outdoors. Specifically, the indoor data rate reaches 1.35 Mbps at 1 m, and it descends to approximately 1.1 Mbps at 8 m. A similar trend is observed outdoors, though with a slightly lower data rate. Anyway, the sensor is able to transmit at a rate higher than 1 Mbps when the client distance is less than 8 m, which is adequate for periodic defect detection of power equipment in industrial plants.

To meet the bandwidth requirement of AE measurement, the sampling rate of the sensor is set to 500 kHz. So a measurement data set of 50 k samples (16 bit per sample) requires about 0.8 s to be transmitted at a data rate of 1 Mbps. Considering 0.1 s measurement duration, the total time of a complete measurement would be only 0.9 s approximately.

C. Energy Consumption

Energy consumption is another crucial parameter for wireless sensors since it affects the battery life and, therefore, the interval between sensor maintenance. The microcontroller has several optimized modes for reducing power consumption, moreover, the firmware is designed so that it remains in sleeping mode for most of time reducing the current to few microamperes. Periodically, the chip awakes for BLE advertisement taking current impulses of about 10 mA within a very short time. A higher power consumption is expected during RF transmission. The authors decide to utilize a direct way to measure the current as shown in Fig. 9. The voltage on a 1 Ω shunt resistor cascaded between battery and PCB is employed to perform the current measurement.

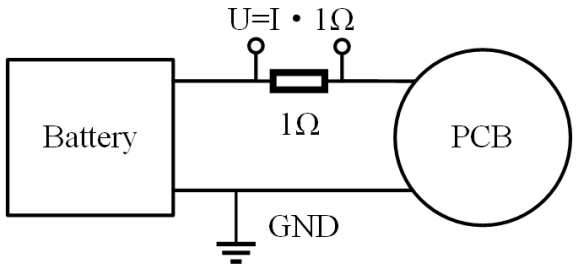


Fig. 11. The current measurement diagram.

The energy consumption of the wireless sensor operations primarily includes advertisement, connection event, ADC measurement, DAC self-calibration and RF transmission. The currents of each operation are shown in Fig. 12. In order to estimate the battery life, the charge is used to describe energy consumption, charge cost of each operation could be calculated by Eq. (3):

$$Q = \int_0^T idt \tag{3}$$

Therefore, it is easy to estimate the charges for these operations as follows: 24 μC for advertisement Q_{adv}, 2 μC for connection event Q_{Con}, 0.1 μC for each ADC measurement Q_{adc}, 0.6 μC for each DAC self-calibration Q_{dac}, and 17.25 mC for each RF data transmission Q_{RF}. Since the Q_{adc} and the Q_{dac} are very small, they are negligible in the following calculation.

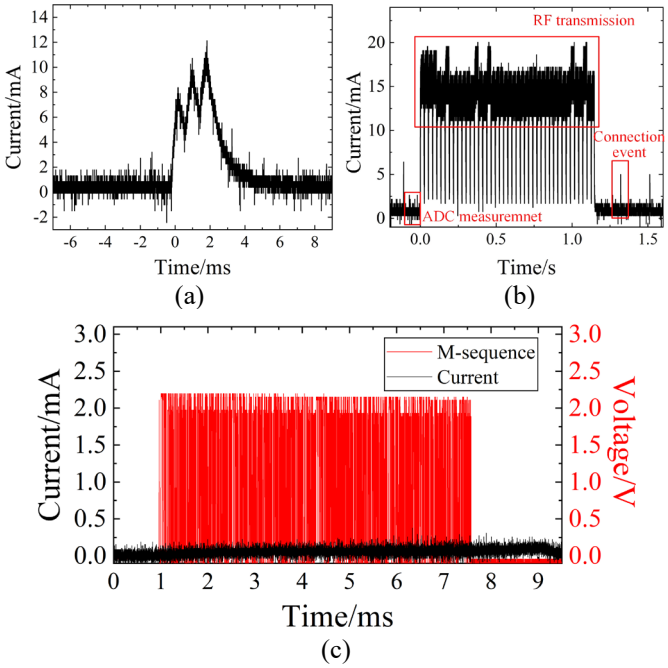


Fig. 12. Currents of the five main operations. (a) Advertisement. (b) ADC measurement, RF data transmission and connection event. (c) DAC.

For monitoring mode with the fastest data rate, if the sensor advertises every 10 s and makes one measurement every 10 min, the estimated charge per hour Q_{1h} would be:

$$Q_{1h} = n_{adv} \times Q_{adv} + n_{Con} \times Q_{Con} + 6 \times Q_{RF} \tag{4}$$

where n_{adv} and n_{Con} represent the number of advertisement and connection events per hour. Thus, the Q_{1h} is about 112.26 mC. Since the battery CR 2477 has a nominal capacity of 1 A·h (3600 C), the theoretical lifetime can be estimated as around 4 years. However, considering a real situation, the operative life is lower than this value due to battery self-discharge and capacity reduction for environmental parameters, but a practical lifetime of approximately one year is feasible.

IV. THE VIBRATION-AE COMBINED WIRELESS SENSOR NETWORK

A. Framework of the WSN

The framework of the vibration-AE combined WSN, consisting of 3 terminals, is shown in Fig. 13.

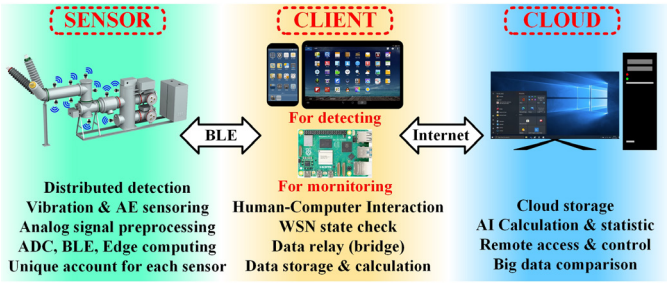


Fig. 13. Framework of the Vibration-AE Combined WSN

The sensor terminal is the measurement component that comprises multiple wireless vibration-AE combined sensors which are responsible for collecting, processing and transmitting combined signals from various positions on the equipment. Each sensor has a unique identifier code (UIC) which is the only key to access its exclusive account on the cloud service, all the data about the sensor could be found in its cloud account. Even when the sensor is damaged or lost, we can remake a new sensor to replace it, and all the historical data could be inherited.

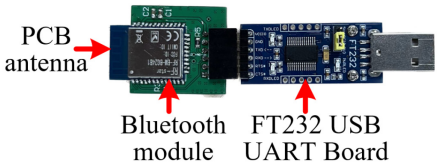
The client terminal serves as a bridge between the sensor and cloud terminals in this system, communicating with the sensors by BLE and with the cloud by internet, it features human-computer interaction, WSN state check (Battery power, connected sensor number, etc.) as well as local data storage and computing. For detecting mode, the PC or smartphone with APP is employed to configure the measurement, such as sampling number, sampling frequency, etc. This mode is useful for periodical on-site measurement by experienced staff, the WSN will work once the user sends notifications. For monitoring mode, a dedicated BLE receiver powered stably and connected to the internet is installed around the field, so the user can remotely interact with it. After setting up the monitoring parameters, the WSN will automatically measure and upload the data periodically.

The cloud terminal works as the central hub for storage and analysis within the system. It saves the Transducer Electronic Data Sheets (TEDS) and historical data uploaded from all sensors, offering powerful computational capabilities. Each sensor has a unique account that records TEDS and historical data results. The TEDS includes parameters such as vibration and AE calibration sensitivity, working band, amplification, and measurement range. Historical data comprises original data, vibration frequency spectrum, PD number and upload times, etc. The main objective of the cloud terminal is to extract features from this extensive data to evaluate the mechanical and insulation condition of the power equipment.

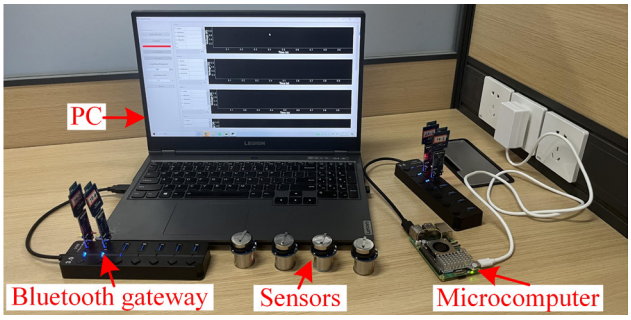
B. Prototype of the WSN

Generally, a BLE host can connect with a maximum of seven slaves, which limits the WSN's function and scalability. Besides, when a host connects to multiple slaves, it might lead to data blocking and unstable connection, resulting in low efficiency of the WSN. To address this issue, multiple BLE hosts can be added to a single client. This approach alleviates the transmission load on each host and increases the number of nodes that can be connected simultaneously.

Fig. 14 (a) describes the designed Bluetooth gateway, which communicates with the sensor nodes via the EFR32BG24 Bluetooth module and with the client via the FT232 USB UART board. But alternative setup can be used as well. Fig. 14 (b) shows 4 sensor nodes connect with 4 Bluetooth gateways, two of which controlled by the client PC and the other two controlled by the client microcomputer. In this case, since the BLE employs the Frequency Hopping Spread Spectrum (FHSS), multiple Bluetooth gateways do not interfere with each other. This allows clients to achieve reliable synchronized communication and measurement across multiple sensor nodes.



(a)



(b)

Fig. 14. The developed vibration-AE combined WSN. (a) The designed Bluetooth gateway. (b) A prototype of the WSN.

Users can do detection work on the client side. For the monitoring mode, this paper proposes two measurement ways.

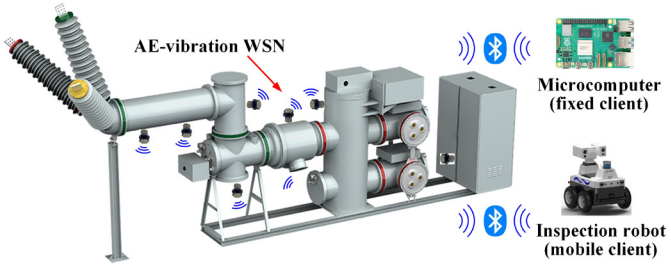


Fig. 15. Two monitoring clients for power equipment.

As shown in Fig. 15, the fixed client, consisting of a single-board computer and Bluetooth gateways, is powered by a stable power supply and is fixed near the equipment being tested. It controls the sensors within the area to measure and upload data to the internet. Besides, the mobile client (Inspection robot), equipped with Bluetooth gateways, performs inspection throughout the entire substation. It controls the sensors to measure the equipment nearby and then proceeds to measure the next area. Therefore, the fixed client can monitor the equipment in real-time but requires a stable power supply, which is suitable for online monitoring of key

equipment or areas. The mobile client can inspect the entire substation but requires some time to reach the specified equipment area for measurement, and the robots can do other tasks at the same time. It is suitable for periodic monitoring of multiple equipment or areas.

V. The Experiment in Laboratory and Application in Actual GIS Substation

A. A Vibration –PD joint experiment

A vibration and metal particle PD joint experiment is carried out to verify the measurement performance of the combined sensor and to demonstrate the fusion analysis of vibration and AE signals. The experiment platform is shown in Fig. 16. which is designed to simulate metal particle PD under vibration that could occur in a GIS. There is a pot with a high voltage electrode and ground plane, AC high voltage source is used to provide a high electric field, and a vibration exciter can generate vibration. The wireless sensor is fixed on the ground of the pot to measure signal.

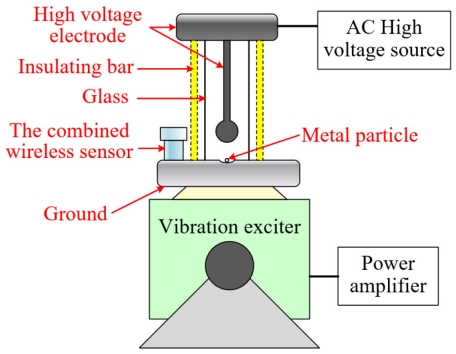


Fig. 16. Vibration – metal particle PD joint experiment

When the AC high voltage rises more than partial discharge inception voltage (PDIV), the metal particle starts to jump, attracted by electric field force. When the particle falls back to the ground, the PDs occur to generate AE signal. In this experiment, a metal particle with a diameter of 2 mm is placed inside the SF_6 pot with 0.45 MPa pressure to simulate actual particle PD in GIS [35]. In order to simulate the vibration on actual GIS equipment during operation (vibration frequency 100 Hz, vibration amplitude 0.02 g ~ 0.5 g [36].), the vibration exciter provides accelerations of 0.1 g and 0.3 g at 100 Hz. Besides, the AC voltage is set to 10.4 kV to simulate the electrical field in GIS.

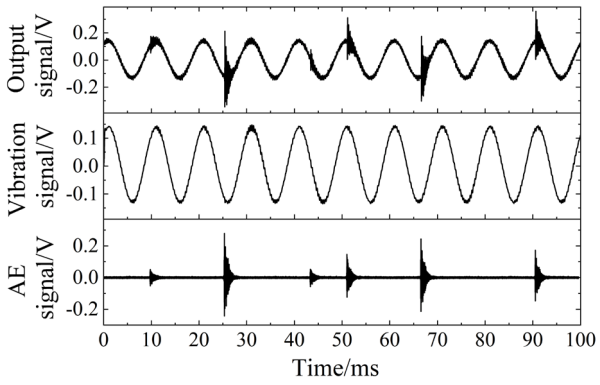


Fig. 17. The combined signal and separated signals.

Fig. 17 shows the output signal from the wireless sensor. There are some PD pulses on the vibration. It is clear that the signal has different frequency components, thus, the combined signal should be separated by edge computing to obtain the vibration signal and PD signal.

To further study the relation between vibration and PD signals, a novel Vibration-AE Amplitude (VAA) graph is presented in this paper which records PD amplitudes on Y axis and the corresponding vibration amplitudes at PD's timeing on X axis. Fig. 18 shows the VAA graphs recording for 64 s under 0.1 g vibration and 0.3 g vibration respectively. It can be seen that the PD occurring at the vibration peaks is more dense, which is statistically illustrated in TABLE V. The PD number occurring at high vibration amplitude is approximately 2000, at medium vibration amplitude is about 1200, and at low vibration amplitude is about 1000. In addition, under 0.3 g vibration, the PDs amplitudes rise as the vibration amplitudes increase (the blue dotted line), while this phenomenon is not clear under 0.1 g vibration. In conclusion, the PDs are prone to occur at high vibration amplitude, and higher vibration can generate PDs with greater amplitudes than low vibration.

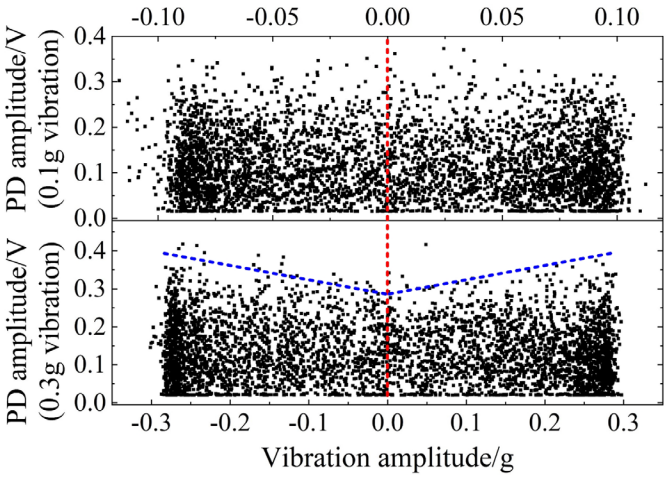


Fig. 18. The VAA graphs under 0.1 g and 0.3 g vibration.

In Fig. 19 (a), the first quarter of a 100 Hz vibration cycle is analyzed as an example due to its symmetry. The duration t_1, t_2, and t_3 correspond to acceleration amplitude ranges of 0~1/3A, 1/3A~2/3A, and 2/3A~A, respectively. The ratio, t_1: t_2: t_3, is 1:1.15:2.48, which approximately euqals to the PD number ratio for the same amplitude ranges under vibration amplitudes of 0.1 g or 0.3 g. Although PD events occur uniformly in the time domain, the amplitude range 2/3A~A accounts for 54% of the vibration cycle. This is attributable to the intrinsic properties of sinusoidal vibration signals, where the time intervals associated with amplitudes near the peak occupy a larger proportion of the cycle. Consequently, regardless of the vibration peak amplitude, the VAA graph displays dense distribution of PD signals at both ends of the graph and sparse distribution in the middle.

The energy of a metal particle during a collision is proportional to the PD amplitude [37]. However, energy conservation does not apply to this process because the vibration is externally powered. During a collision, the particle's energy, combined with energy from the external

vibration, is redistributed into heat, AE, and changed particle energy, as described in Eqs. (5) and (6):

$$\Delta E = E_p - E_{Vib} = \frac{1}{2} m_p v_p^2 - \frac{1}{2} m_{Vib} v_{Vib}^2 \quad (5)$$

$$\Delta E \rightarrow E_H + E_A + E_p^{'} \quad (6)$$

where E_p, E_{vib} represent the particle's pre-collision energy, and the energy of the vibration platform, m_p and m_{vib} correspond to the masses of the particle and the vibration platform, respectively, and v_p and v_{vib} are their respective velocities. Furthermore, E_H represents thermal energy, E_A corresponds to the energy of AE, and E_p' denotes the changed energy of the particle after the collision.

The particle collision process is inherently complex, however, this study focuses on the moment immediately before the collision. In Fig. 19 (b), when a collision occurs at the vibration peak, the velocity of the vibration platform is zero, so ΔE equals E_p without -E_{vib}, resulting in a relative large E_A (AE). while when the collision occurs at the vibration zero-crossing point, the vibration's velocity v_{vib} is at its maximum, so the ΔE would be reduced, the E_A generated by collision decreases, resulting in V shape distributation (blue dotted line in Fig. 18).

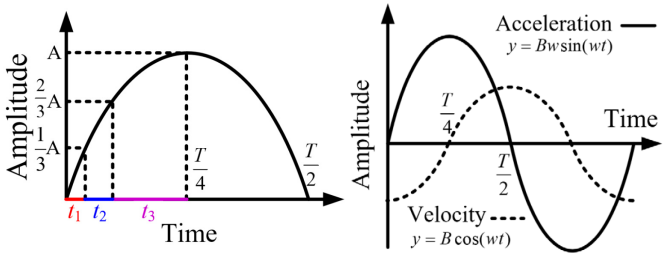


Fig. 19. The principle analysis of VAA graph. (a) Time proportion of vibration acceleration amplitude range. (b) Acceleration and velocity of external vibration.

TABLE V
PD NUMBER STATISTIC

Statistical range (0.1 g vibration)	PD number	Statistical range (0.3 g vibration)	PD number
$\|x\|\leq 0.033$ g	1019	$\|x\|\leq 0.1$ g	970
0.033 g$<|x|\leq$0.066 g	1216	0.1 g$<|x|\leq$0.2 g	1193
$|x|>$0.066 g	2090	$|x|>$0.2 g	2150

B. Application of the WSN in GIS substation

In this section, the WSN is applied to detect the voltage transformer gas chamber of a 220 kV GIS, which contains metering and protection devices, such as circuit breaker, disconnector, and current transformer. Some operations can cause changes in GIS mechanical structure, resulting in defects such as loosening, poor contact, and winding deformation, etc. The experiment site is shown in Fig. 20. There are three-phase voltage transformer gas chambers (A, B, C), with two sensors installed horizontally at the middle of each gas chamber, since the vibration at the middle of gas chamber is relative large and stable which can be usually used for analysis. The six sensors work synchronously.

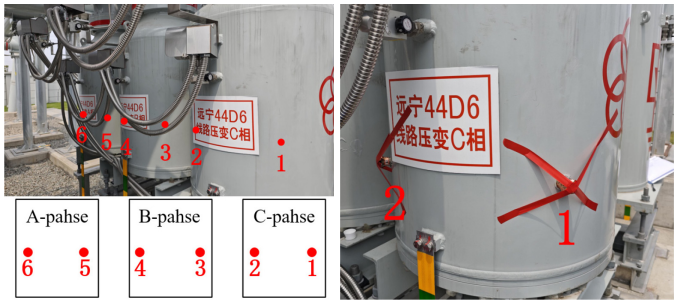
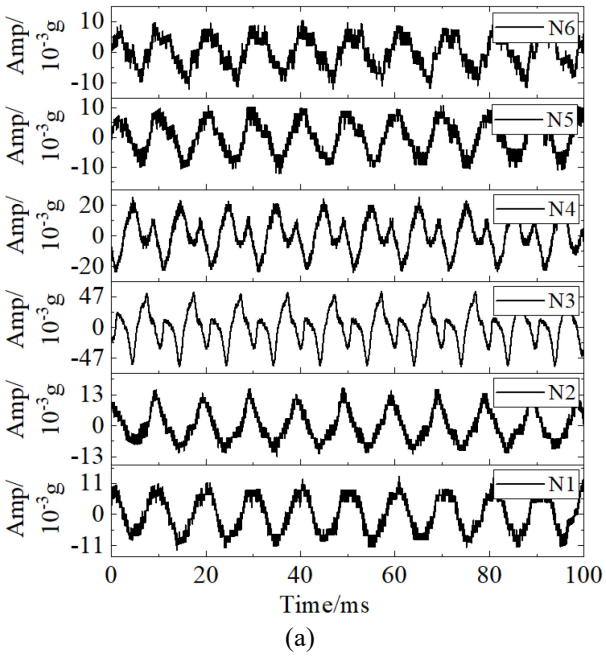


Fig. 20. The Experiment on a voltage transformer gas chamber of a 220 kV GIS. (a) Sensors arrangement points. (b) Sensors installation.



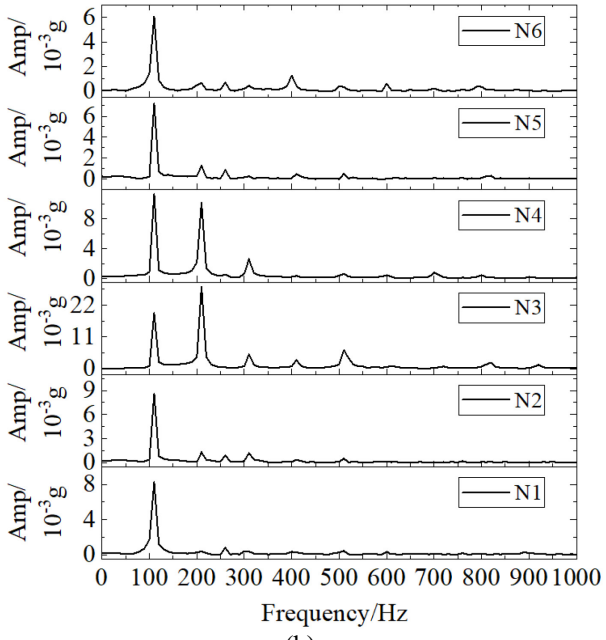


Fig. 21. The signals on a voltage transformer gas chamber of a 220 kV GIS. (a) Signals of six sensor nodes in the time domain. (b) Signals of sensor nodes in the frequency domain.

The experimental results are shown in Fig. 21 (a), which records output signals of the six sensors. It can be seen that the vibration signal waveforms on the A and C phase enclosures are 100 Hz sine waves, while the vibration signal of the B phase shows a significant abnormal waveform. Fig. 21 (b) shows the spectrum information obtained through FFT transformation. It is clear that sensor nodes 1, 2, 5, and 6 mainly exhibit a 100 Hz vibration acceleration component with an amplitude of approximately 7×10^{-3} g. In contrast, node 3 measures 100 Hz and 200 Hz vibration components with amplitudes of 19×10^{-3} g and 28×10^{-3} g respectively, and node 4 contains 100 Hz and 200 Hz vibration components with amplitudes of 12×10^{-3} g and 10×10^{-3} g respectively.

It is verified that under normal condition, the vibration on GIS equipment is periodical with minimal interference, the vibration frequencies are concentrated around the 100 Hz fundamental frequency, while vibration signals at other frequency points are nearly zero. In addition, the vibration of GIS three phases are similar, which can be used to compare and analyze horizontally. However, when poor contact occurs, some 100 Hz harmonic frequencies (200 Hz, 300 Hz, etc) start to occur, and the poorer the contact, the greater the amplitudes of these harmonic frequencies. In this paper, 100 Hz and 200 Hz vibration are clearly measured by the sensors on B-phase, therefore, it is preliminarily determined that the B-phase chamber might have a poor contact defect, which could potentially develop into a floating discharge [38-40].

VI. Conclusion

This article develops a reliable smart vibration-AE combined WSN intended for mechanical and insulation defects detection of power equipment.

The wireless sensor comprises a vibration-AE combined measurement component and a designed PCB which enables main functions such as impedance self-calibration, analog processing, edge computing, BLE transmission, and data storage. Performance tests indicate that the vibration sensitivity is 510 mV/g and the AE sensitivity exceeds 70 dB; the data rate remains above 1 Mbps within 8 m distance, both indoors and outdoors. Energy consumption tests show that the operational life is estimated to be at least 1 year. The proposed M-sequence self calibration method could acquire almost the same inpedance curve with the impedance analyzer, but consuming less time and energy. A vibration-AE combined WSN is introduced and established to measure vibration and AE signals of the power equipment, two client modes are presented for different mornitoring applications. Furthermore, the vibration and PD joint experiment results verify the effective measurement performance of the sensor, the vibration-AE fusion signal can be acquired, separated computed, a novel VAA graph is proposed to explore the correlation between metal particle PD and vibration, indicating that metal particle PDs concentrate on vibration peak, and greater vibration could increase the amplitude of the PD. The application of the WSN on an actual 220 kV GIS equipment shows the abnormal vibration (200 Hz) on chamber B-phase indicate there is poor contact inside, further demonstrating practicability and efficiency of the WSN.

The proposed WSN features vibration-AE measurement, low power consumption and cost, long operational life, and intelligent edge processing, these characteristics make it suitable for continuous and distributed on-field monitoring of power equipment. Future work will focus on more experimental validation and fusion analysis with intelligent algorithms to enhance the system's performance and reliability.

Acknowledgment

The authors would like to thank all the reviewers and the editors for their valuable suggestions for improving this article.

References

[1] M. Majid et al., “Applications of Wireless Sensor Networks and Internet of Things Frameworks in the Industry Revolution 4.0: A Systematic Literature Review,” Sensors, vol. 22, no. 6, p. 2087, Mar. 2022.

[2] L. Lombardo, M. Parvis, S. Corbellini, C. E. Arroyave Posada, E. Angelini, and S. Grassini, “Environmental monitoring in the cultural heritage field⋆,” The European Physical Journal Plus, vol. 134, no. 8, Aug. 2019.

[3] C. -J. Chou and C. -H. Chen, “Measurement and analysis of partial discharge of high and medium voltage power equipment,” 2018 7th International Symposium on Next Generation Electronics (ISNE), 2018, pp. 1-4.

[4] M. Ren, C. Zhang, M. Dong, Z. Xiao and A. Qiu, “Partial discharges triggered by metal-particle on insulator surface under standard oscillating impulses in SF6 gas,” in IEEE Transactions on Dielectrics and Electrical Insulation, vol. 22, no. 5, pp. 3007-3018, October 2015.

[5] J. Hao, Y. Ding, Y. Li, X. Li, X. Jiang and H. Peng, “Comparative Analysis of Partial Discharge and Mechanical Vibration Characteristics under Loose Bus Base with Foreign Body Defect of GIS,” 2022 IEEE International Conference on High Voltage Engineering and Applications (ICHVE), 2022, pp. 1-4.

[6] S. Bagheri, Z. Moravej and G. B. Gharehpetian, “Classification and Discrimination Among Winding Mechanical Defects, Internal and External Electrical Faults, and Inrush Current of Transformer,” in IEEE Transactions on Industrial Informatics, vol. 14, no. 2, pp. 484-493, Feb. 2018.

[7] H. D. Ilkhechi and M. H. Samimi, “Applications of the Acoustic Method in Partial Discharge Measurement: A Review,” in IEEE Transactions on Dielectrics and Electrical Insulation, vol. 28, no. 1, pp. 42-51, February 2021.

[8] Y. -B. Wang et al., “Acoustic localization of partial discharge sources in power transformers using a particle-swarm-optimization-route-searching algorithm,” in IEEE Transactions on Dielectrics and Electrical Insulation, vol. 24, no. 6, pp. 3647-3656, Dec. 2017.

[9] M. Iorgulescu, R. Beloiu and M. O. Popescu, “Vibration monitoring for diagnosis of electrical equipment's faults,” 2010 12th International Conference on Optimization of Electrical and Electronic Equipment, 2010, pp. 493-499.

[10] Y. Zhong, J. Hao, Y. Ding, R. Liao, H. Xu and X. Li, "Novel GIS Mechanical Defect Simulation and Detection Method Based on Large Current Excitation With Variable Frequency," in IEEE Transactions on Instrumentation and Measurement, vol. 71, pp. 1-15, 2022, Art no. 3519815.

[11] Y. Shi, S. Ji, F. Zhang, Y. Dang and L. Zhu, “Application of Operating Deflection Shapes to the Vibration-Based Mechanical Condition Monitoring of Power Transformer Windings,” in IEEE Transactions on Power Delivery, vol. 36, no. 4, pp. 2164-2173, Aug. 2021.

[12] H. Xu, C. Meng, Q. Huang, C. Luo, J. Zhang and Z. Liu, "Time-frequency Vibration Characteristics Analysis of Disconnectors of GIS Equipment with Poor Contact Mechanical Defect," 2021 IEEE 5th International Conference on Condition Assessment Techniques in Electrical Systems (CATCON), Kozhikode, India, 2021, pp. 215-219.

[13] L. Ma et al., "Study on the PD Creeping Discharge Development Process Induced by Metallic Particles in GIS," 2020 IEEE International

Conference on High Voltage Engineering and Application (ICHVE), Beijing, China, 2020, pp. 1-4.

[14] X. Ge, H. Ji, X. Cui and C. Li, "Movement Behavior and Partial Discharge of the Single Metallic Particle in GIS at Operated Voltage," in IEEE Transactions on Plasma Science, vol. 47, no. 9, pp. 4319-4328, Sept. 2019.

[15] X. Li, W. Liu, D. Ding and Y. Xu, "Metal Particle Movement and Induced Insulator Flashover Under Impact Vibration Generated By Switching Operation in GIS," in IEEE Transactions on Power Delivery, vol. 38, no. 2, pp. 757-766, April 2023.

[16] T. Xie, X. Huang and S. -K. Choi, "Intelligent Mechanical Fault Diagnosis Using Multisensor Fusion and Convolution Neural Network," in IEEE Transactions on Industrial Informatics, vol. 18, no. 5, pp. 3213-3223, May 2022.

[17] A. Stief, J. R. Ottewill, J. Baranowski and M. Orkisz, "A PCA and Two-Stage Bayesian Sensor Fusion Approach for Diagnosing Electrical and Mechanical Faults in Induction Motors," in IEEE Transactions on Industrial Electronics, vol. 66, no. 12, pp. 9510-9520, Dec. 2019.

[18] S. Shao, R. Yan, Y. Lu, P. Wang and R. X. Gao, "DCNN-Based Multi-Signal Induction Motor Fault Diagnosis," in IEEE Transactions on Instrumentation and Measurement, vol. 69, no. 6, pp. 2658-2669, June 2020.

[19] A. Secic, M. Krpan and I. Kuzle, "Vibro-Acoustic Methods in the Condition Assessment of Power Transformers: A Survey," in IEEE Access, vol. 7, pp. 83915-83931, 2019.

[20] Y. Zhang, K. Feng, H. Ma, K. Yu, Z. Ren and Z. Liu, "MMFNet: Multisensor Data and Multiscale Feature Fusion Model for Intelligent Cross-Domain Machinery Fault Diagnosis," in IEEE Transactions on Instrumentation and Measurement, vol. 71, pp. 1-11, 2022, Art no. 3526311.

[21] R. Zhao, G. Jiang, Q. He, X. Jin and P. Xie, "Current-Aided Vibration Fusion Network for Fault Diagnosis in Electromechanical Drive System," in IEEE Transactions on Instrumentation and Measurement, vol. 73, pp. 1-10, 2024, Art no. 3510010.

[22] S. Li *et al*., "Design and Prototyping of a Combined Sensor for Vibration and Temperature Measurement in High-Temperature Environments," in IEEE Transactions on Instrumentation and Measurement, vol. 73, pp. 1-9, 2024, Art no. 9512809.

[23] H. Wang, X. Zhang, X. Han, Y. Sun, H. Chen and J. Li, "A Novel Composite Sensor for Overvoltage and UHF Partial Discharge Measurement in GIS," in IEEE Transactions on Power Delivery, vol. 37, no. 6, pp. 5476-5479, Dec. 2022.

[24] X. Zhao and P. Wang, "A Deployable Edge Computing Solution for Machine Condition Monitoring," 2024 IEEE International Instrumentation and Measurement Technology Conference (I2MTC), Glasgow, United Kingdom, 2024, pp. 1-6.

[25] J. Wang, P. Fu, L. Zhang, R. X. Gao and R. Zhao, "Multilevel Information Fusion for Induction Motor Fault Diagnosis," in IEEE/ASME Transactions on Mechatronics, vol. 24, no. 5, pp. 2139-2150, Oct. 2019.

[26] C. Zhao, B. Tang, Y. Huang and L. Deng, "Edge Collaborative Compressed Sensing in Wireless Sensor Networks for Mechanical Vibration Monitoring," in IEEE Transactions on Industrial Informatics, vol. 19, no. 8, pp. 8852-8864, Aug. 2023.

[27] T. Xie, X. Huang and S. -K. Choi, "Intelligent Mechanical Fault Diagnosis Using Multisensor Fusion and Convolution Neural Network," in IEEE Transactions on Industrial Informatics, vol. 18, no. 5, pp. 3213-3223, May 2022.

[28] Z. Zhang, L. Lombardo, T. Shi, X. Han, M. Parvis and J. Li, "A Smart Combined Wireless Sensor for Vibration and AE Signals Measurement," 2024 IEEE International Instrumentation and Measurement Technology Conference (I2MTC), Glasgow, United Kingdom, 2024, pp. 1-6.

[29] T. Abderrahmane, A. Nourredine, and T. Mohammed, "Experimental analysis for comparison of wireless transmission technologies: Wi-Fi, Bluetooth, ZigBee and LoRa for mobile multi-robot in hostile sites," International Journal of Power Electronics and Drive Systems/International Journal of Electrical and Computer Engineering, vol. 14, no. 3, p. 2753, Jun. 2024.

[30] Methods for the calibration of vibration and shock transducers - Part 21: Vibration calibration by comparison to a reference transducer, ISO 16063-21:2003.

[31] Non-destructive testing-Acoustic emission inspection-Secondary calibration of acoustic emission sensors, ISO 12714:1999.

[32] Z. Zhang et al., "A Novel IEPE AE-Vibration-Temperature-Combined Intelligent Sensor for Defect Detection of Power Equipment," in IEEE Transactions on Instrumentation and Measurement, vol. 72, pp. 1-9, 2023, Art no. 9506809.

[33] Y. Luo, J. Gao, P. Chen, L. Hu, Y. Shen and L. Ruan, "A test method of winding deformation excited by pseudorandom M-Sequences — Part I: Theory and simulation," in IEEE Transactions on Dielectrics and Electrical Insulation, vol. 23, no. 3, pp. 1605-1612, June 2016.

[34] Janů P, Bajer J, Dyčka P, et al. "Precise experimental determination of electrical equivalent circuit parameters for ultrasonic piezoelectric ceramic transducers from their measured characteristics," Ultrasonics, 2021, 112: 106341.

[35] L. Dai, "Insulation Fault Analysis Caused by Internal Metal Particles in 330kV GIS," 2024 IEEE 7th Advanced Information Technology, Electronic and Automation Control Conference (IAEAC), Chongqing, China, 2024, pp. 1722-1735.

[36] Feng Ying, Li Xu, Zhong Yao, et al. "Research on mechanical defect diagnosis method of GIS equipment based on multi-layer fusion vibration data analysis," Proceedings of the CSEE, vol. 44, no. 14, pp. 5797-5810, 2024.

[37] Li Jie, Li Xiaoang, Lv Yufang, et al. "Motion characteristics of free metal particles in GIS under sinusoidal vibration excitation," Transactions of China Electrotechnical Society, 2021, 36(21): 4580-4589+4597.

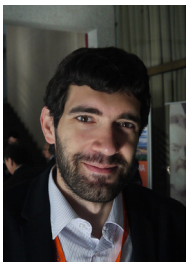
[38] Y. Liu et al., "Connection state diagnosis method of GIS disconnector based on mechanical vibration," High Voltage Eng., 2019, vol. 45, no. 5, pp. 1591–1599.

[39] J. Zhang, H. Xu, X. Wang, Y. Ding, X. Dai and J. Hao, "Mechanical Defect Field Detection for Operational GIS Equipment Based on Vibration Signal Analysis," 2021 6th Asia Conference on Power and Electrical Engineering (ACPEE), Chongqing, China, 2021, pp. 1244-1248.

[40] H. Wang, J. Yang, X. wang, F. Li, W. Liu and H. Liang, "Feature Fingerprint Extraction and Abnormity Diagnosis Method of the Vibration on the GIS," 2020 IEEE International Conference on High Voltage Engineering and Application (ICHVE), Beijing, China, 2020, pp. 1-4.



Zhaoyu Zhang, was born in Yuncheng, Shanxi, China, in 1995. He received the M.S. degree in electrical engineering from Xi'an Jiaotong University, Xi'an, in 2020. He is currently pursuing the double Ph.D. degree in electrical engineering with Xi'an Jiaotong University, Xi'an, China and Politecnico di Torino, Turin, Italy. His main fields of interest are the intelligent sensing technology, fault detection and state evaluation for power equipment.



Luca Lombardo (Member, IEEE) received the B.S. degree and the M.S. in Electronic Engineering, respectively, in 2014 and 2016 from the University of Messina, Messina (Italy). He received the Ph.D. degree in Metrology from the Politecnico di Torino, Turin (Italy) in 2019. He is Assistant Professor in the measurement and instrumentation field with the Department of Electronics and Telecommunications at Politecnico di Torino, Turin (Italy). His research interests includes the development of innovative sensors and systems, embedded systems and measurement instrumentation, especially in the fields of environmental monitoring, biomedical applications and cultural heritag



Tianyi Shi was born in 2000. He received the B.Sc. degree in electrical engineering from Xi'an Jiaotong University, Xi'an, in 2022, where he is currently pursuing the M.S. degree with a focus on the intelligent sensing technology, fault detection and state evaluation for power equipment.



Xutao Han was born in Xi'an, Shaanxi, China, in 1991. He received the B.Sc. and Ph.D. degrees in electrical engineering from Xi'an Jiaotong University, Xi'an, in 2013 and 2019, where he is currently a Research Assistant with a focus on the smart sensor technology and detective and diagnostic techniques for electrical equipment.



Marco Parvis (Fellow, IEEE) was born in Italy, in 1958. He received the M.S. degree in electrical engineering and the Ph.D. degree in metrology from the Politecnico di Torino, Turin, Italy, in 1982 and 1987, respectively. He is currently a Full Professor of electronic measurements with the Politecnico di Torino, where he was the Dean of the II Faculty of Engineering. His main fields of interest are intelligent instrumentation, application of signal processing to measurement, biomedical, and chemical measurements. He has authored more than 100 publications.



Junhao Li (Senior Member, IEEE) was born in Xuchang, Henan, China, in 1980. He received the Ph.D. degree in electrical engineering from Xi'an Jiaotong University, Xi'an, China, in 2010. He is currently a Professor with Xi'an Jiaotong University, where he is involved in the detective and diagnostic techniques for electrical equipment and new types of the test method for electrical equipment, etc.